Improved Droop Controller for Distributed Generation Inverters in Islanded AC Microgrids

Mohamed Islam Grairia[1*], Riad Toufouti[1]

[1] Department of Electrical Engineering, Faculty of Science and Technology, Laboratory of Electrical and Renewable Energies LEER, Souk Ahras University, 41000 Souk Ahras, P.O.B. 1553, Algeria
[*] Corresponding author, e-mail: m.grairia@univ-soukahras.dz

Abstract

Stability in island microgrids is crucial for efficient power distribution among distributed generation (DG) inverters. Conventional droop control, while effective in power sharing, poses challenges with voltage stability due to frequency and voltage deviations resulting from changing load power. Such deviations can lead to system instability, impacting power flows within each inverter. Therefore, this paper introduces a proposed droop control approach that effectively tackles the issues of frequency and voltage deviation, aiming to restore them to their rated values and significantly enhance transient response in power flows among inverters. The novel method incorporates integrating controllers for frequency and voltage, coupled with the utilization of virtual impedances. These virtual impedances, comprising virtual positive/negative-sequence impedance (VPI/VNI) loops at the fundamental frequency and a virtual harmonic impedance (VHI) loop at harmonic frequencies, play a crucial role in overcoming mismatched line impedance conditions, ultimately improving overall system performance. Simulation results demonstrate the effectiveness and outstanding performance of inverters operating in parallel within an island AC microgrid. The proposed approach ensures stable voltage and frequency levels in all operational states, regardless of varying load conditions.

Keywords

droop control, distributed generation, virtual impedance, voltage-controlled inverters, power-sharing

1 Introduction

Conventional energy production worldwide heavily relies on fossil fuel sources such as diesel, fuel, and gas to meet the growing demand for electricity. However, this dependence has led to the depletion of non-renewable resources and significant environmental damage. As a result, there is a pressing need for distributed generation (DG) systems that harness power from renewable sources [1, 2]. DG systems offer the advantage of providing reliable electricity through solar, wind, and other renewable resources [3]. Nevertheless, the seamless integration of these renewable resources within the microgrid and their synchronization with the utility grid present a significant challenge.

A microgrid provides a solution for addressing the challenges associated with DG units, serving as a link between distributed renewable resources and the utility grid. It consists of DG units that can operate autonomously or in conjunction with the grid, depending on the mode. In AC microgrids, inverters are used to connect DG units to the AC distribution system, as shown in Fig. 1. To ensure
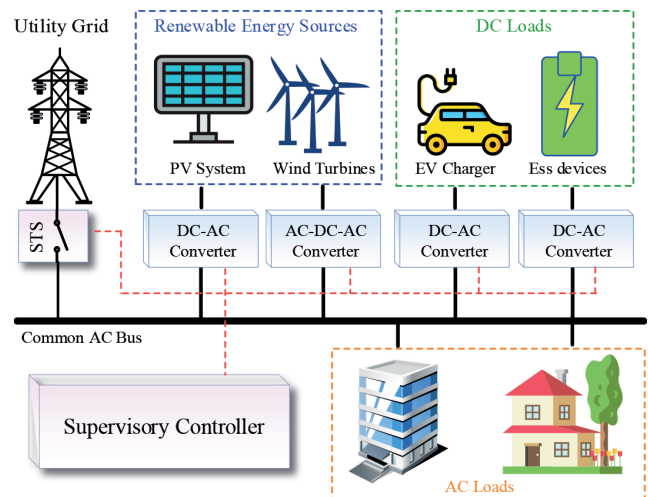

Fig. 1 Schematic of an AC microgrid

efficient and reliable power flow, various control strategies have been developed and implemented. These strategies focus on regulating power sharing among the DG units and delivering high-quality power within the microgrid,

which can be classified into two commonly used control schemes: The first scheme employs a communication system among parallel-connected inverters, including popular methods such as the master-slave control method [4–7], the average current-sharing method [8–10], and circular chain control [11]. While these schemes effectively control output voltage and power sharing, their reliance on communication links can compromise system reliability. An alternative approach is the second type of control, which utilizes droop control [12–15]. This technique efficiently shares load power among parallel-connected inverters by utilizing the active and reactive power flows to regulate the frequency and amplitude of the output voltage without the need for inter-inverter communication. With each inverter relying solely on local measurements, this method provides higher flexibility and reliability, particularly in terms of the physical positioning of the units.

Nevertheless, the conventional droop technique has a certain number of drawbacks [13], including the fact that mismatched line impedance has a significant impact on power-sharing accuracy, slow transient response, inadequate adjustment of harmonic power when nonlinear loads are supplied, and that the droop characteristics lead to a decrease in the voltage amplitude and frequency of each inverter. Addressing the decoupling of active and reactive power in AC microgrids presents a significant challenge, leading to the exploration of various solutions. One approach tackles this challenge by introducing an inductor or resistor in series with the inverter output, modifying the overall equivalent impedance to be either inductive ($P-F/Q-E$) or resistive ($P-E/Q-F$). However, this inclusion of components increases both the cost and size of the inverter, primarily due to the required physical space. To overcome these drawbacks, virtual impedance techniques [16] have emerged as a promising solution. These techniques leverage rapid control loops to mitigate line impedance mismatches without incurring power losses. However, it's important to note that integrating virtual impedance alongside the inherent deviations associated with droop control may reduce the output voltage from individual inverters. To effectively compensate for voltage and frequency deviations within the microgrid, secondary control assumes a crucial role [17]. Operating at a higher level than primary control (droop control with the virtual impedance), this mechanism aims to maintain stability and ensure the high-quality delivery of power. By actively monitoring system parameters, the secondary control system swiftly responds to deviations, fostering a stable and reliable power supply within the microgrid.

To address the aforementioned drawbacks and enhance load sharing, a proposed droop approach is implemented, providing control over the output voltage and restoring the frequency and amplitude voltage deviations of each inverter to their specified values. This approach is characterized by a rapid transient response, enabling seamless adaptation to load changes. Furthermore, the limitation of mismatched line impedance is effectively resolved through the implementation of virtual impedance using the combination of the current component extraction method with the summing approach, which will be discussed in detail later in the paper.

The paper is organized as follows: Section 2 offers an overview of the power flow of the conventional droop control technique. Section 3 introduces a comprehensive set of techniques and methodologies. including the decomposition of current components, the calculation of fundamental positive power, the implementation of double loop voltage and current control, selective virtual impedance implementation, and the proposed droop control technique. Section 4 shows the simulation results conducted using the MATLAB/Simulink environment. Finally, the paper concludes in Section 5.

2 Theory of droop controller

Droop control is a technique used to emulate the behavior of synchronous generators in order to achieve power-sharing among parallel-connected inverters. Inspired by the behavior of synchronous generators, droop control adjusts the output frequency and voltage of each inverter in response to changes in load conditions.

Fig. 2 depicts the equivalent circuit of two parallel inverters coupled to an alternating current bus through different output impedances. The load current should preferably be divided equally between the two inverters. However, when the equivalent output impedances of the two inverters
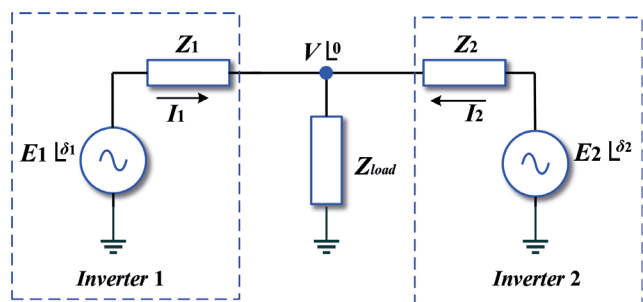

Fig. 2 Operation of two parallel inverters connected to AC bus

differ, the power shared between them becomes inaccurate. The active and reactive power transmitted to the common AC bus can be represented as follows [18]:

$$\begin{cases} P = \dfrac{EV}{Z}\cos(\theta-\delta) - \dfrac{V^2}{Z}\cos(\theta-\delta) \\ Q = \dfrac{EV}{Z}\sin(\theta-\delta) - \dfrac{V^2}{Z}\sin(\theta-\delta) \end{cases}, \qquad (1)$$

where V and E are the amplitudes of the microgrid bus voltage and the inverter output voltage, δ indicating the phase angle between the microgrid bus voltage and the output voltage of the inverter. Z and θ are the amplitude and the angle of the output impedance, respectively.

Due to the large inductor filter and high inductive line impedance, it is expected that the inverter output impedance is entirely inductive, $Z = j X$ ($\theta = 90°$) where X is the output reactance of the inverter, and hence, it is possible to express the active and reactive powers applied to the AC bus by:

$$\begin{cases} P = \dfrac{EV}{X}\sin(\delta) \\ Q = \dfrac{EV}{X}\cos(\delta) - \dfrac{V^2}{X} \end{cases}. \qquad (2)$$

In general, the power angle δ is extremely low (sin (δ) = δ and cos (δ) = 1). It is obvious that the active power is strongly influenced by the phase angle, whereas the reactive power is mostly dependent on the amplitude of the inverter voltage. Therefore, the majority of paralleled-inverter wireless controls use the conventional droop method, which results in droops in the frequency and amplitude of the inverter output voltage. As a result, the characteristics defining the droop properties of $P−F$ and $Q−E$ as shown in Fig. 3 can be given by:

$$\begin{cases} F = F_o - k_f (P - P_o) \\ E = E_o - k_v (Q - Q_o) \end{cases}, \qquad (3)$$

where F_o and E_o represent the output voltage frequency and amplitude with no load, k_f and k_v represent the coefficients
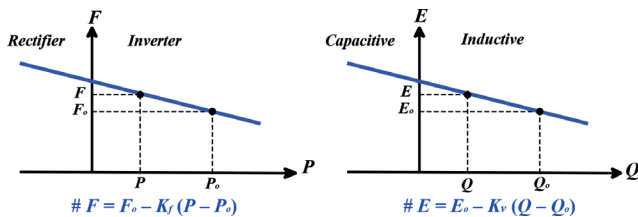
for the drop frequency and amplitude, which are calculated as follows:

$$\begin{cases} k_f = \dfrac{\Delta F}{P_{max}} \\ k_v = \dfrac{\Delta E}{Q_{max}} \end{cases}, \qquad (4)$$

where ΔF and ΔE are the maximum allowed deviations in frequency and voltage, respectively. P_{max} and Q_{max} are the maximal active and reactive power delivered from the inverter, respectively.

In low voltage power, the line impedance becomes nearly resistive $Z = R$ ($\theta = 0°$), which leads to a change in P and Q power flow expressions and becomes:

$$\begin{cases} P = \dfrac{EV}{R}\cos(\delta) - \dfrac{V^2}{R} \\ Q = -\dfrac{EV}{R}\sin(\delta) \end{cases}. \qquad (5)$$

The active power is clearly influenced by the inverter voltage amplitude, while the reactive power is primarily influenced by the phase angle. As a consequence, the formulas for $P−E/Q−F$ droop can be expressed by:

$$\begin{cases} F = F_o + k_f (Q - Q_o) \\ E = E_o - k_v (P - P_o) \end{cases}. \qquad (6)$$

As a result, a control strategy based on the $P−F/Q−E$ droop control must be implemented for inductive output impedance, whereas the $P−E/Q−F$ droop strategy is applied for resistive impedance.

3 System configuration

Fig. 4 depicts the detailed configuration of an island microgrid that comprises two parallel DG units linked to the AC bus, each with a different line impedance. The power stage of each DG unit consists of a DC link, an interface inverter, and an LC filter. Additionally, both DG units are equipped with a primary controller, which incorporates the droop control technique, virtual impedance, as well as voltage and current control.

3.1 Current component decomposition

In order to enhance power calculations and enable effective implementation of virtual impedance, a combination of three key blocks is utilized: a harmonic decoupling network (HDN), parallel dual second-order generalized integrator-quadrature signal generation (DSOGI-QSG),
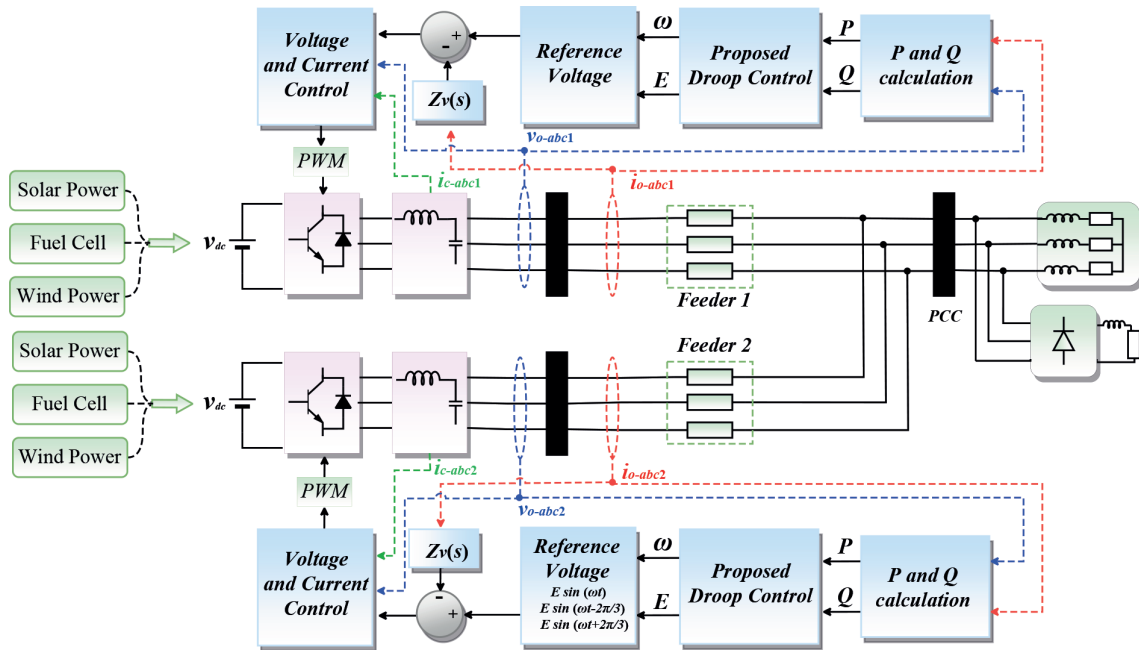

Fig. 3 $P−F$ and $Q−E$ droop characteristic

Fig. 4 Block diagram of the control scheme for two parallel distributed generation units in islanded mode

and positive-negative sequence calculation (PNSC). These blocks collaborate harmoniously to ensure the precise extraction of important components from the output current. This includes accurately isolating the fundamental positive and negative sequence currents as well as the dominant harmonic currents [19]. The overall signal extraction structure is illustrated in Fig. 5.

Initially, as a fundamental step in the signal processing chain, the HDN is introduced. This mechanism incorporates a cross-feedback structure that separates and manages the interactions among the various harmonics present in the input current signal, followed by the DSOGI-QSGs, which are finely tuned at distinct frequencies and operate concurrently to effectively separate various current components. Each DSOGI-QSG comprises two SOGI-QSGs that function in parallel, as depicted in Fig. 5(b). The implementation of the SOGI-QSG allows for the extraction of both in-phase and in-quadrature signals from the input signal [20]. The transfer functions based on closed-loop linking the input i and outputs i' and qi' of the SOGI-QSG are denoted by Eq. (7), and the associated Bode diagrams are shown in Fig. 6.

$$\begin{cases} D(s) = \dfrac{i'(s)}{i(s)} = \dfrac{k\,\omega\,s}{s^2 + k\,\omega\,s + \omega^2} \\[3mm] Q(s) = \dfrac{qi'(s)}{i(s)} = \dfrac{k\,\omega^2}{s^2 + k\,\omega\,s + \omega^2} \end{cases}, \tag{7}$$

Fig. 6 (a) and (b) illustrate that the bandwidth of both the band-pass and low-pass filters is solely influenced by the gain parameter (k) and remains independent of the center frequency (ω). When k decreases, the bandwidth becomes narrower; however, that can lead to slower system responses. It is worth noting that i' is the output version of the band-pass filter of the input i with unit gain and 0° phase shift. On the other hand, the output qi' in Fig. 6(b) represents the low-pass filtered version, characterized by unit gain and a 90° phase shift. For this reason, the structure is referred to as a "quadrature signal generator". Ultimately, the positive sequence component (i^+) and negative sequence component (i^-) can be effectively obtained using the PNSC block, as depicted in Fig. 5 (c).

3.2 Fundamental positive power calculation

Based on the identified current components, the determination of the active and reactive power is carried out by considering the output voltages and the output fundamental positive sequence currents in the $\alpha\beta$ axis as follows [21]:

$$\begin{cases} P = \dfrac{3}{2}\dfrac{\omega_{\mathrm{LPF}}}{s + \omega_{\mathrm{LPF}}}\left(v_{o\alpha} i_{1o\alpha}^+ + v_{o\beta} i_{1o\beta}^+\right) \\[3mm] Q = \dfrac{3}{2}\dfrac{\omega_{\mathrm{LPF}}}{s + \omega_{\mathrm{LPF}}}\left(v_{o\beta} i_{1o\alpha}^+ - v_{o\alpha} i_{1o\beta}^+\right) \end{cases}, \tag{8}$$
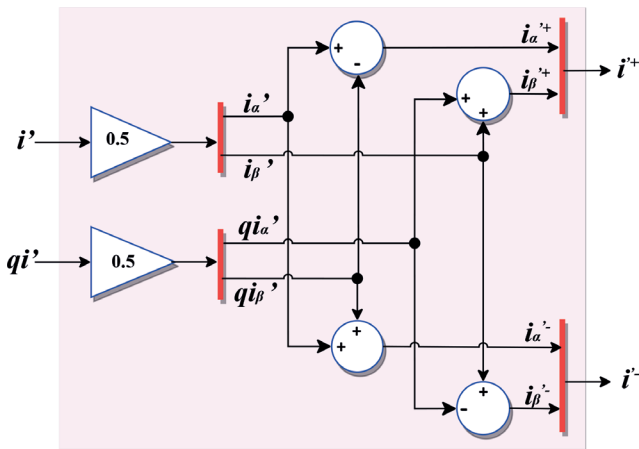
where ω_{LPF} is the cut-off frequency of the low-pass filter (LPF), $i_{1o\alpha}^+$ and $i_{1o\beta}^+$ are fundamental positive sequence output currents. The LPF plays a crucial role in attenuating the undesired ripples present in the active and reactive power signals.
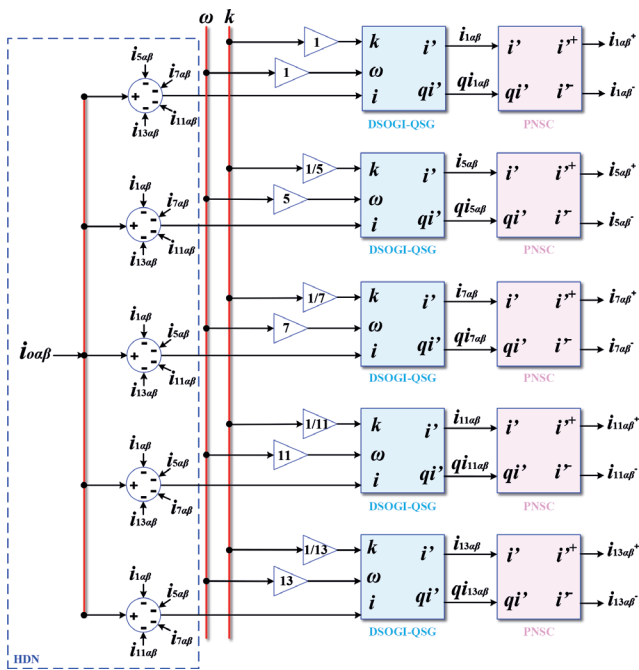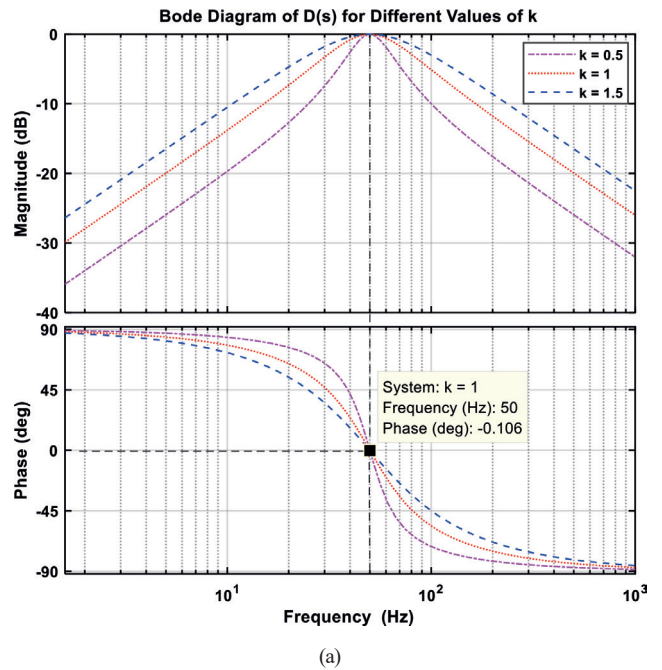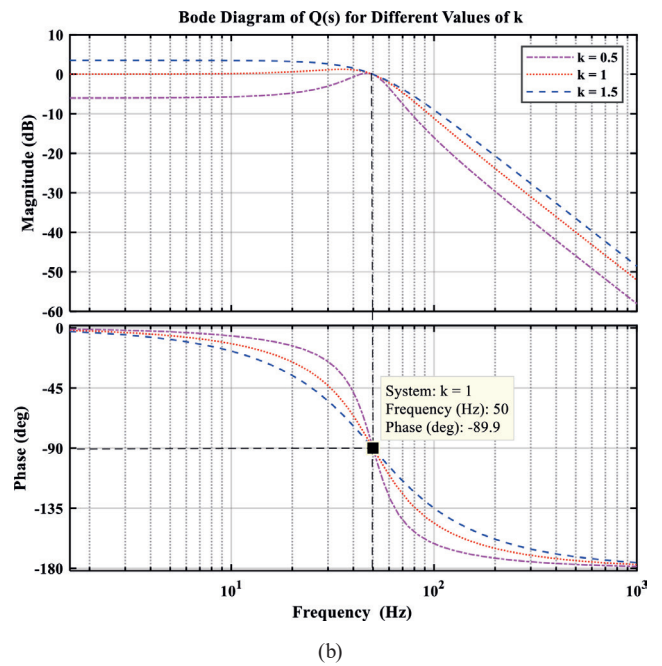
(a)
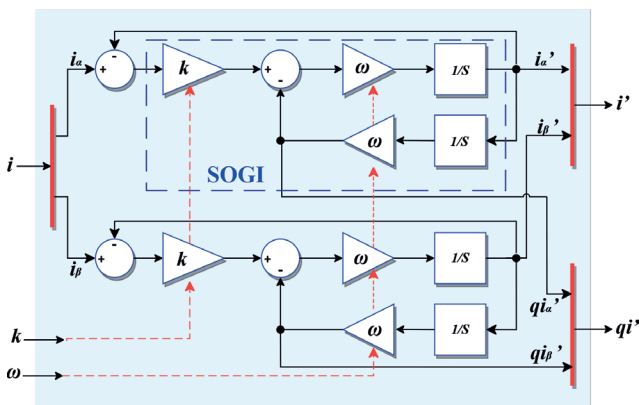
(b)

(c)

Fig. 5 The block diagram illustrates the current signal extraction:
(a) the comprehensive framework; (b) the DSOGI-QSG structure;
(c) the PNSC configuration

(a)

(b)

Fig. 6 Adaptive filter based on SOGI-QSG: (a) $D(s)$ Bode diagram;
(b) $Q(s)$ Bode diagram

3.3 Double loop voltage and current control

Outer and inner control loops are considered by a cascading control that uses the output voltage and the capacitor current. As shown in Fig. 7, the output voltage is used as feedback in the first loop in order to track the reference voltage generated by the droop controller, while the second inner loop uses the current in the capacitor as information to enhance the stability of the system, improve
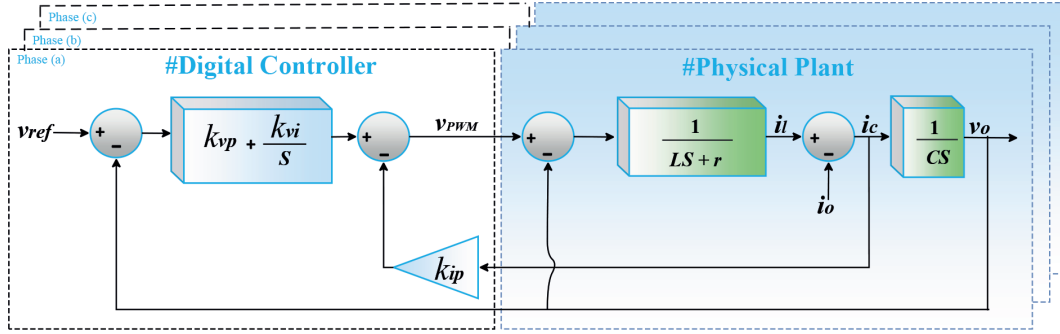
Fig. 7 Double loop voltage and current control

transient response, and provide damping of filter resonance [22]. The output voltage can be given by:

$$v_o = G(s) v_{ref} - Z_o(s) i_o(s), \tag{9}$$

where $G(s)$ is the closed-loop transfer function between v_o and v_{ref} (voltage gain) and $Z_o(s)$ is the closed-loop transfer function between v_o and i_o (output impedance). To determine the expressions of $G(s)$ and $Z_o(s)$, first, assume that i_o is equal to zero, therefore $G(s)$ is given by:

$$G(s) = \frac{v_o}{v_{ref}} = \frac{k_{vp} s + k_{vi}}{\Delta}, \tag{10}$$

where Δ is expressed as:

$$\Delta = LCs^3 + (rC + Ck_{ip})s^2 + (1 + k_{vp})s + k_{vi}. \tag{11}$$

To include a fast transient response and a stable steady-state error, the voltage proportional gain k_{vp} was set to 150 and the integral gain k_{vi} to 50, while the current proportional k_{ip} was adjusted to 60. The steady-state response can be investigated using a $G(s)$ bode diagram, as can be seen in Fig. 8 (a). At a frequency of 50 Hz, the gain is −0.0569 dB, indicating that the amplitudes of the reference voltage and output voltage are identical, while the phase is −0.366 degrees, indicating that the voltage output and voltage reference are in phase.

The closed-loop output impedance must be examined to ensure the decoupling of the power-sharing in parallel operation. The expression for $Z_o(s)$ is obtained by assuming v_{ref} is equal to zero. therefore $Z_o(s)$ is given by:

$$Z_o(s) = \frac{v_o}{i_o} = \frac{Ls^2 + rs}{\Delta}. \tag{12}$$

A Bode diagram in Fig. 8 (b) illustrates the frequency-domain characteristics of the output impedance. It reveals an inductive behavior (89.6°) around the fundamental frequency (50 Hz). This characteristic suggests that the implementation of the $P−F/Q−E$ droop control technique is appropriate in this scenario.
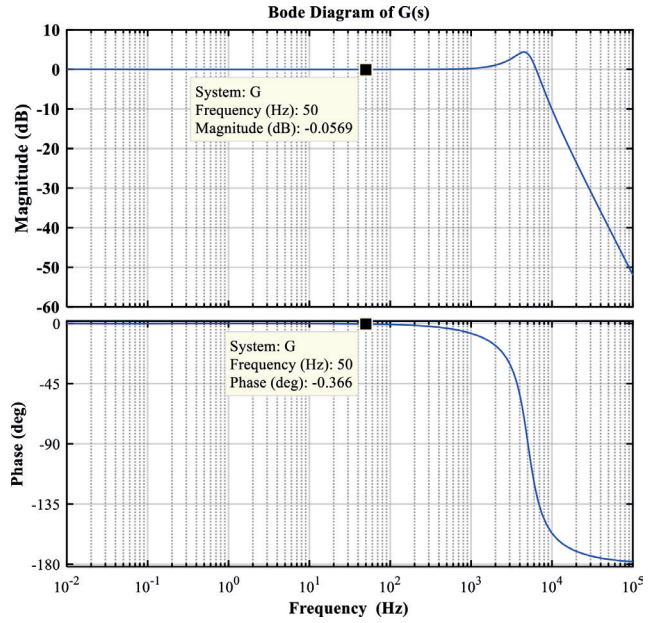
(a)
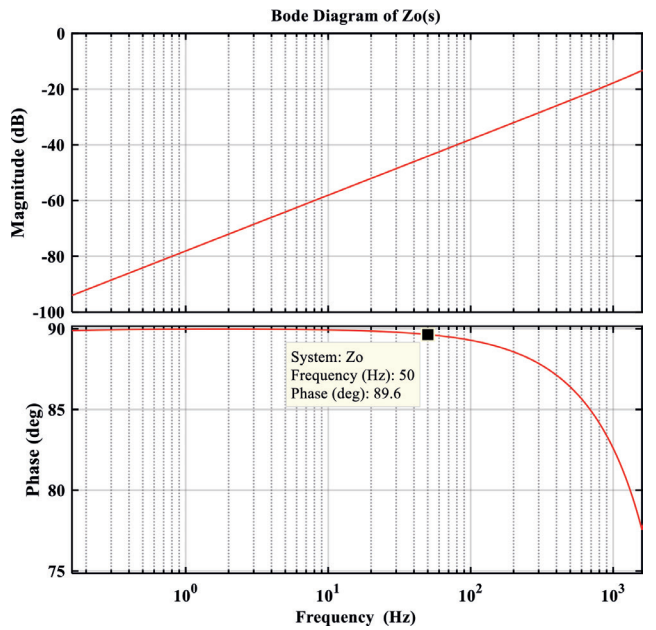
(b)

Fig. 8 Bode diagrams of: (a) voltage gain $G(s)$; (b) output impedance $Z_o(s)$

3.4 Selective virtual impedance implementation

In the context of a microgrid, unbalanced and nonlinear loads pose challenges that introduce components in the point of common coupling (PCC) current, leading to distortion in the output voltage of DG units. The primary objectives are to mitigate this distortion and achieve equitable sharing of current components among the DG units [23]. To address these challenges, the paper suggests the utilization of virtual positive- and negative-sequence impedance, as well as harmonic virtual impedance. These techniques effectively enhance the performance of droop controllers, minimize circulating currents, compensate for voltage distortion, and improve the sharing of harmonic power among the DG units. Furthermore, it has been observed that the output impedance of each DG unit predominantly exhibits inductive characteristics, as discussed previously. However, the accuracy of power control sharing among the DG units is impacted by mismatched line impedance. Therefore, the virtual impedance allows for precise adjustment of the phase and magnitude of the output impedance, ensuring that all DG units perceive an identical output impedance.

The voltage drops occurring at the fundamental positive-negative- sequence and specific harmonic frequencies can be defined by:

$$
\begin{bmatrix} v_{v\alpha,f}^+ \\ v_{v\beta,f}^+ \end{bmatrix} = \begin{bmatrix} R_{v,f}^+ & -\omega_f L_v \\ \omega_f L_v & R_{v,f}^+ \end{bmatrix} \begin{bmatrix} i_{o\alpha,f}^+ \\ i_{o\beta,f}^+ \end{bmatrix},
\tag{13}
$$

$$
\begin{bmatrix} v_{v\alpha,f}^- \\ v_{v\beta,f}^- \end{bmatrix} = \begin{bmatrix} R_{v,f}^- & \omega_f L_v \\ -\omega_f L_v & R_{v,f}^- \end{bmatrix} \begin{bmatrix} i_{o\alpha,f}^- \\ i_{o\beta,f}^- \end{bmatrix},
\tag{14}
$$

$$
\begin{bmatrix} v_{v\alpha,h} \\ v_{v\beta,h} \end{bmatrix} = \begin{bmatrix} R_{v,h} & h\omega_f L_v \\ R_{v,h} & -h\omega_f L_v \end{bmatrix} \begin{bmatrix} i_{o\alpha,h}^h \\ i_{o\beta,h}^h \end{bmatrix},
\tag{15}
$$

where the virtual voltage drops at the fundamental positive- and negative-sequence frequencies are denoted by $v_{v\alpha\beta,f}^+$ and $v_{v\alpha\beta,f}^-$, respectively. Additionally, the virtual voltage drop for the harmonic frequency is represented by $v_{v\alpha\beta,h}$. The variable 'h' is used to indicate the primary harmonic components, such as −5, 7, −11, and 13.

Finally, the total voltage drop associated with the virtual impedance is obtained by adding all of the previously calculated components, as expressed in Eq. 16. The implementation details of the virtual impedance are illustrated in Fig. 9.

$$
\begin{cases} v_{v\alpha} = v_{1\alpha}^+ + v_{1\alpha}^- + v_{5\alpha}^- + v_{7\alpha}^+ + v_{11\alpha}^- + v_{13\alpha}^+ \\ v_{v\beta} = v_{1\beta}^+ + v_{1\beta}^- + v_{5\beta}^- + v_{7\beta}^+ + v_{11\beta}^- + v_{13\beta}^+ \end{cases}.
\tag{16}
$$

To ensure optimal system performance, suitable values for virtual inductance (L_v) and positive virtual resistance $\left(R_{v,f}^+\right)$ are determined using a precise summing approach. Knowledge of the feeders' impedances is crucial for applying this method, enabling the calculation of specific virtual impedance values for each inverter. Obtaining the necessary impedance information for each feeder can be
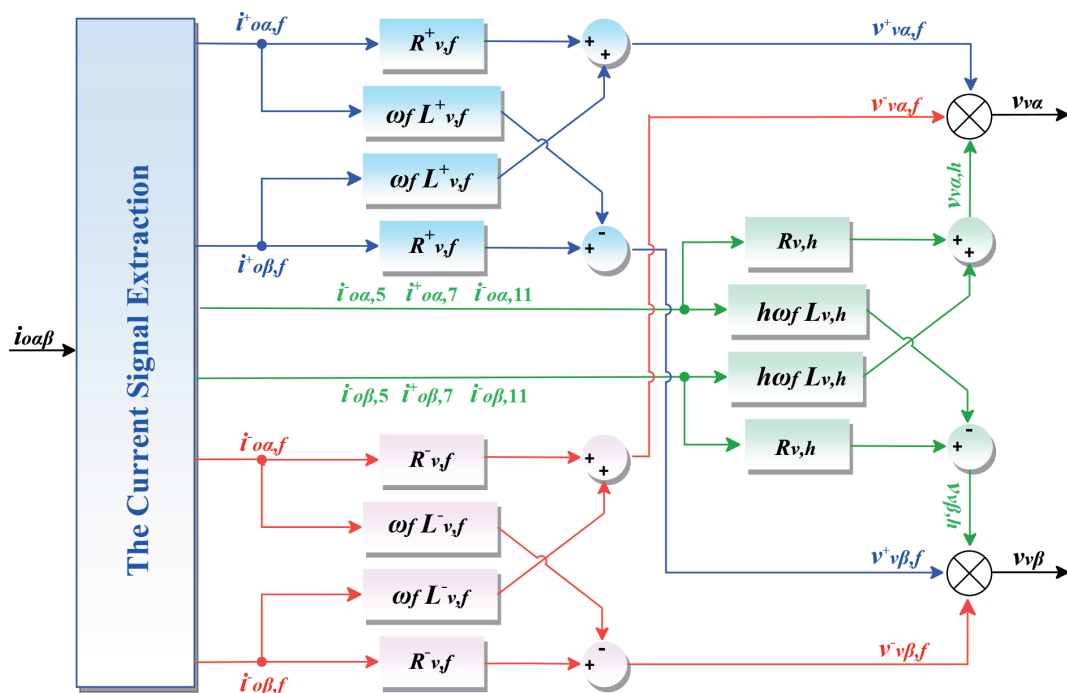

Fig. 9 Selective virtual impedance implementation

achieved through the knowledge of the system's design and cable specifications, while the other employs real-time online impedance estimation techniques, such as the "non-invasive estimation based on the recursive least squares (RLS) algorithm" [24].

The virtual output impedance selection can be accomplished using the summation approach [25, 26], which ensures balanced reactive power sharing by maintaining a consistent voltage drop from each inverter to the AC bus as follows:

$$v_{drop1} = \left(Z_{f1} + Z_{v1} \right) i_{o1} = v_{dropk} = \left(Z_{fk} + Z_{vk} \right) i_{ok}, \tag{17}$$

where $Z_{v1} = R_{v1} + jX_{v1}$ and $Z_{vk} = R_{vk} + jX_{vk}$ represent the virtual output impedance of inverter 1 and the kth inverter, respectively. Similarly, $Z_{f1} = R_{f1} + jX_{f1}$ and $Z_{fk} = R_{fk} + jX_{fk}$ signify the line impedance of inverters 1 and k^{th}.

In the summation approach, one of the virtual output impedances is set to zero, while the remaining virtual output impedances are adjusted to emulate the line impedance. By considering Eq. (17) and assuming that one line impedance is greater than the other ($Z_{f1} > Z_{fk}$), we can select Z_{v1} to be zero. Hence, tuning the optimal values of virtual impedances in a system with multiple inverters, ranging from the first to the kth inverter, as follows:

$$\begin{cases} Z_{v1} = 0 \\ Z_{v2} = Z_{f1} - Z_{f2} \\ \dots \\ Z_{vk} = Z_{f1} - Z_{fk} \end{cases} \tag{18}$$

As a result, the values of L_v and $R_{v,f}^+$ can be expressed in the following manner:

$$\begin{cases} L_{vk} = \dfrac{X_{f1}}{\omega} - \dfrac{X_{fk}}{\omega} \\ R_{v,fk}^+ = R_{f1} - R_{fk} \end{cases} \tag{19}$$

Moreover, to introduce damping in the system, smaller virtual resistances are specifically chosen for the fundamental negative sequence $\left(R_{v,f}^- \right)$ and selected harmonic frequencies ($R_{v,5}$, $R_{v,7}$, $R_{v,11}$ and $R_{v,13}$).

3.5 The proposed droop control technique

The variation in load power led to deviations in each inverter's output voltage amplitude and frequency. To ensure voltage quality and high precision of active and reactive power distribution, a proposed droop control uses the difference frequency ($F - F_o$) and the difference voltage ($E - E_o$) as information with integrator control k_m and k_n

respectively to restore the deviation frequency and amplitude of the output voltage to their rated values. Fig. 10 shows the proposed method for controlling the active and reactive power. The frequency and amplitude of the inverter's voltage reference are expressed as follows:

$$\begin{cases} F = \dfrac{k_m}{s + k_m} F_o - \dfrac{s k_f}{s + k_f} \left(P - P_o \right) \\ E = \dfrac{k_n}{s + k_n} E_o - \dfrac{s k_v}{s + k_v} \left(Q - Q_o \right) \end{cases}, \tag{20}$$

where k_m and k_n are the integrator coefficients of frequency and amplitude voltage, respectively.

4 Simulation results and discussion

To validate the proposed control, two DG inverters operating in parallel, as shown in Fig. 4, were built and tested. The loads are connected to a 380 V (line-to-line RMS), 50 Hz AC bus, and the system parameters are listed in Table A1 in the Appendix.

4.1 Proposed control against linear load

Four different scenarios were investigated to assess the performance of the proposed control strategy in the context of linear RL load with an initial active power of 6 kW and reactive power of 3 kVAR. In the first scenario, the proposed control was applied without the inclusion of virtual impedance for $t < 0.5$ s. Subsequently, in the second scenario, starting at $t \geq 0.5$ s, the virtual impedance was enabled. To figure out how the load will be affected by the proposed control strategy, at $t = 1$ s, the active and reactive powers of the load were increased to 10 kW and 5 kVAR, respectively. Following that, in the fourth scenario, at $t = 1.5$ s, the load powers were returned to their initial conditions of 6 kW active power and 3 kVAR reactive power. The simulation results for this case are shown in Figs. 11 (a)–(h).
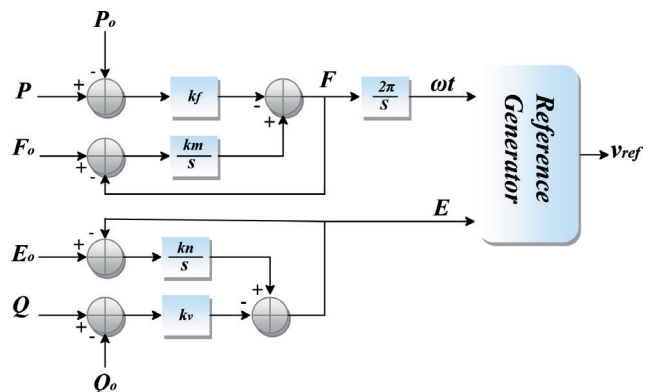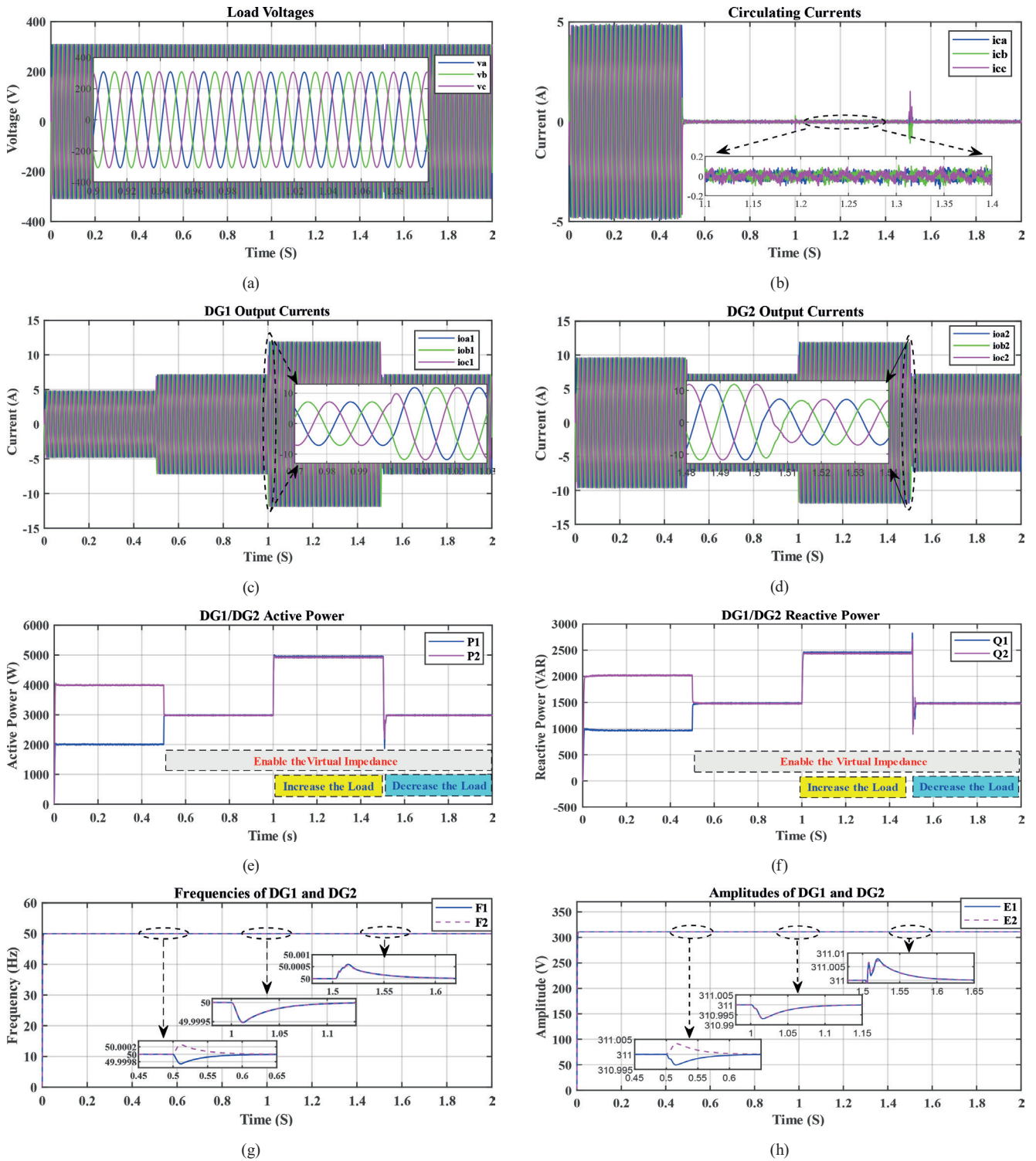

Fig. 10 Proposed droop control

Fig. 11 The results of the first test: (a) load voltages; (b) Circulating currents; (c) DG1 output currents; (d) DG2 output currents; (e) DG1/DG2 active power; (f) DG1/DG2 reactive power; (g) DG1/DG2 frequency response; (h) DG1/DG2 amplitude response

As observed in Fig. 11 (a), the voltage of the load remains stable across all scenarios, exhibiting a consistent frequency of 50 Hz and a steady amplitude of 311 V (phase to ground). This indicates that the proposed control strategy effectively maintains voltage stability throughout the different load variations.

In Figs. 11 (c) and (d), it is evident that there is an initial disparity in the currents supplied by the inverters, leading to the emergence of circulating currents. Nonetheless, upon enabling the virtual impedance at $t = 0.5$ s, the currents equalize, resulting in a substantial reduction in the circulating current to a range of $[-0.2$ A, 0.2 A],

as depicted in Fig. 11(b). This highlights the effectiveness of the virtual impedance strategy in minimizing circulating currents between the inverters.

Fig. 11 (e)–(f) depict the behavior of the system power under different load steps. Initially, there is a decoupling between the active and reactive powers. However, the power-sharing between the two inverters is inequitable due to mismatched line impedances. Nevertheless, with the enablement of the virtual impedances at $t = 0.5$ s, each DG inverter provides half of the total required power to the load, ensuring equitable power sharing. Notably, as the load power increases at $t = 1$ s to 10 kW of active power and 5 kVAR of reactive power, each DG inverter promptly responds by increasing its power output to meet the load requirements. This fast transient response demonstrates the resilience of the control system. Similarly, when the load power decreases at $t = 1.5$ s to 6 kW of active power and 3 kVAR of reactive power, the control system effectively adjusts the power delivered from each DG according to load changes.

The performance of the proposed droop control strategy in regulating the output frequency and amplitude of each DG unit is highlighted in Fig. 11 (g) and (h). When active power increases at $t = 1$ s, there is a Slight frequency deviation, quickly returning to its nominal value. Similarly, an increase in reactive power causes a minor amplitude decrease, which is promptly restored to its nominal value. Conversely, at $t = 1.5$ s, as both active and reactive power decrease, the frequency shows a temporary increase before converging back to the nominal value. Additionally, a decrease in reactive power leads to a slight amplitude increase, subsequently returning to the nominal value. These observations indicate that the proposed droop control effectively maintains the nominal frequency and amplitude values for each DG unit without any steady-state deviation.

4.2 Proposed control against non-linear load

The second test evaluates the effectiveness of the proposed control strategy when dealing with a non-linear load. In this case, the non-linear load is represented by a diode-bridge rectifier with $R_{nl} = 50\ \Omega$ and $L_{nl} = 1$ mH. During the initial period ($t < 0.5$ s), the virtual impedance is not applied. However, from $t \geq 0.5$ s, the virtual impedance becomes active. The simulation results for this test are shown in Figs. 12 and 13.

In Fig. 12 (a) and (b), it is evident that despite the presence of distorted current from the non-linear load, the voltage at the AC bus remained stable in both frequency and amplitude throughout the entire test.

To thoroughly validate the proposed scheme, the amplitude of each order of harmonic current obtained by the signal extraction block is presented in Figs. 12 (c)–(h). The results reveal that the proposed scheme evenly distributes each order of harmonic current. This demonstrates the reliability of the proposed approach in addressing various types of harmonics and ensuring balanced current sharing.

In order to gain a comprehensive understanding of the currents supplied by each Distributed Generator and the method for extracting their positive sequence, which is subsequently used to calculate active and reactive power for droop control, we refer to Fig. 13 (a) and (c). These figures illustrate the currents delivered by the DGs, revealing the presence of high harmonics. On the other hand, Fig. 13 (b) and (d) demonstrate the positive sequence extractions, displaying a sinusoidal waveform with significantly low Total Harmonic Distortion (THD). This indicates that the proposed method effectively extracts the positive sequence from the currents, ensuring accurate power calculations and enhancing the droop control performance with reduced harmonic distortion and ripples.

4.3 Disconnection and reconnection of the DG unit

In this test, the primary focus is on investigating the dynamic behavior of the power system under the disconnection and reconnection of a DG unit. At $t = 0.3$ s, DG2 is disconnected from the microgrid. Following this, at $t = 0.6$ s, DG2 is reintegrated into the microgrid. The simulation results for these tests are depicted in Fig. 14 (a)–(d), respectively.

Fig. 14 (a) and (b) illustrate the active and reactive power supplied by each DG unit. Initially, both DG units delivered equal power to the load. However, at $t = 0.3$ s, DG2 is disconnected, prompting DG1 to increase its active and reactive power output to fulfill the load demand. Upon DG2's reconnection at $t = 0.6$ s, the load power is equally shared between the two DG units.

The frequency and amplitude responses of the output voltage for each DG unit are depicted in Fig. 14 (c) and (d). Whenever DG2 is disconnected, DG1 lowers its frequency to increase active power output and reduces its amplitude voltage to increase reactive power output. On the other hand, when DG2 is connected, DG1 increases its frequency to decrease active power output and raises its amplitude voltage to decrease reactive power output. This relationship demonstrates that an increase in active power is accompanied by a decrease in frequency, while
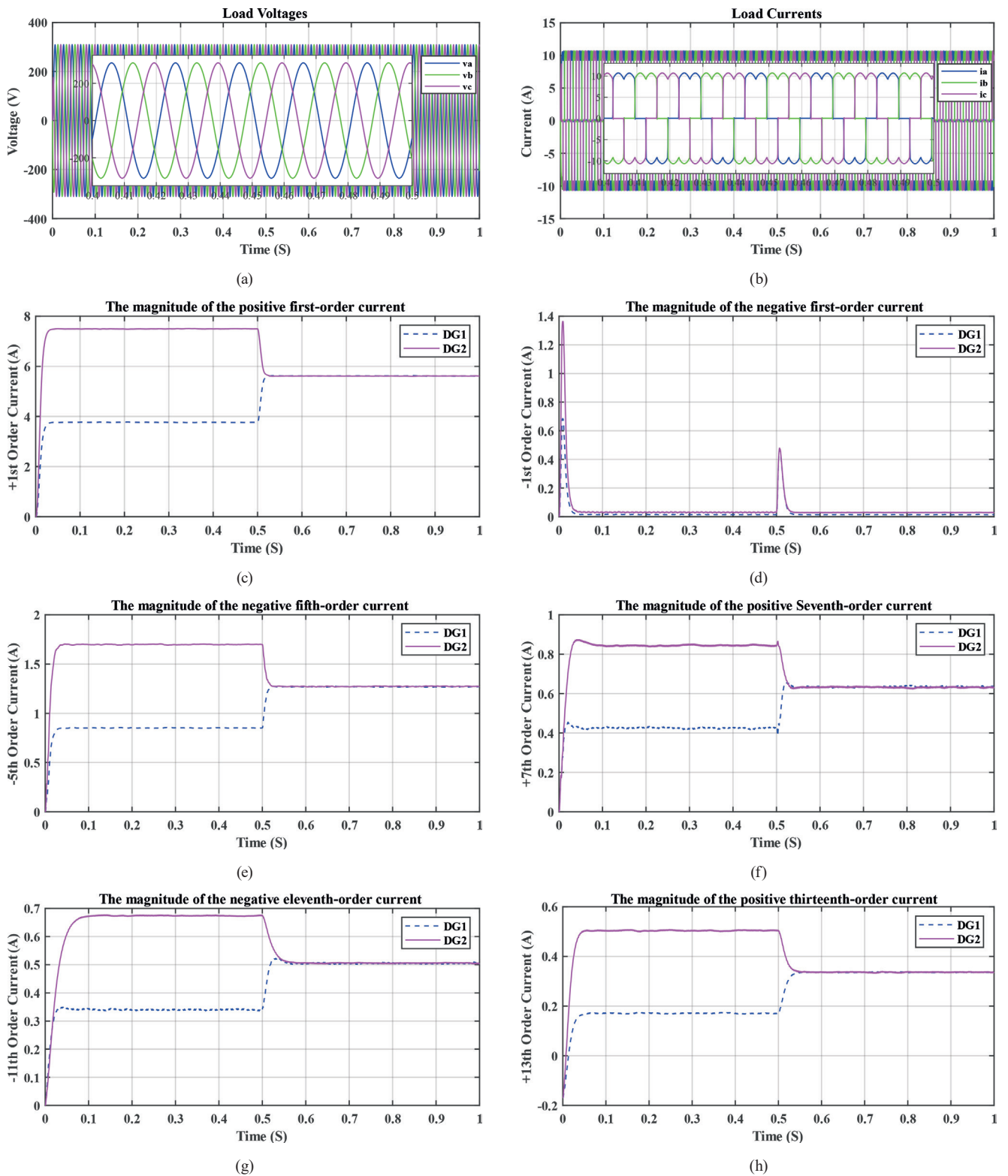
Fig. 12 The results of the second test: (a) load voltages; (b) load currents; (c) fundamental positive sequence current; (d) fundamental negative sequence current; (e) fifth order negative sequence harmonic current; (f) seventh order positive sequence harmonic current; (g) eleventh order negative sequence harmonic current; (h) thirteenth order positive sequence harmonic current
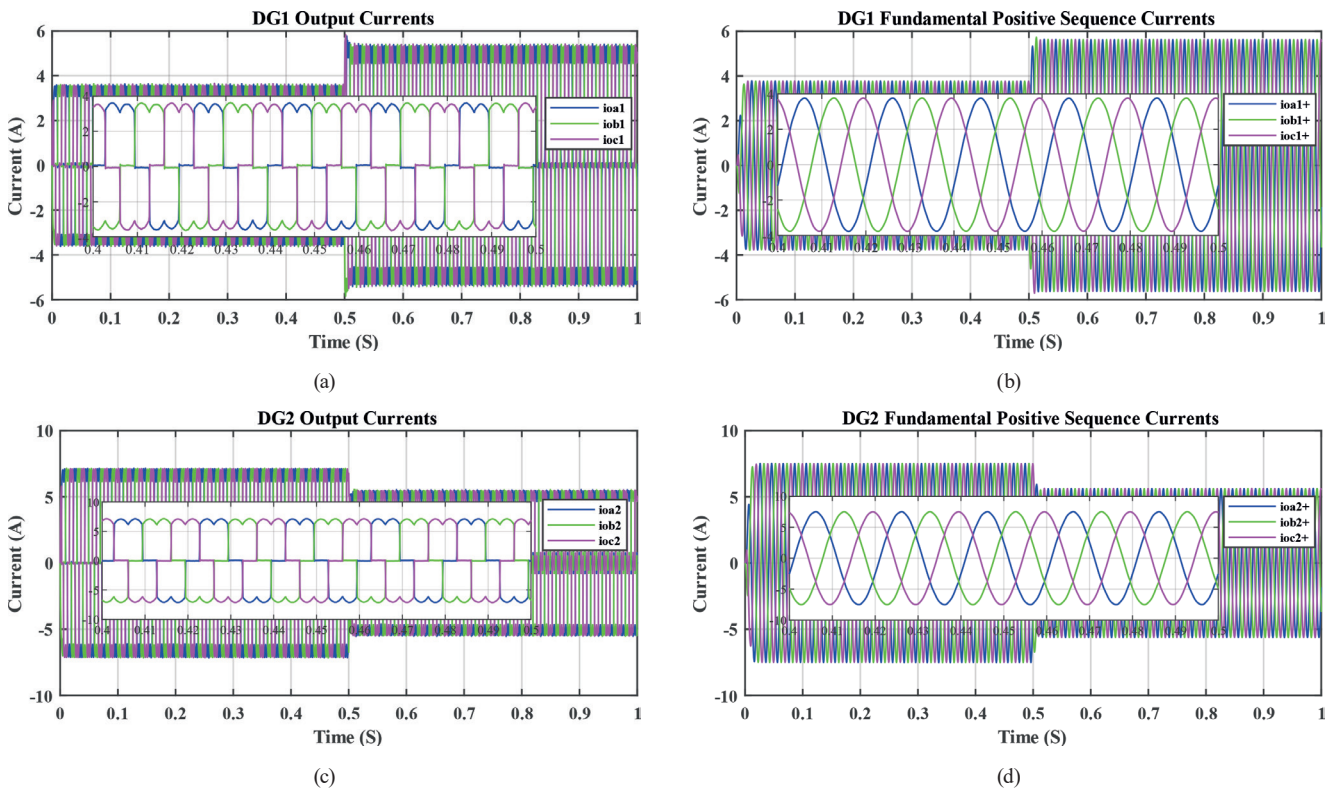
Fig. 13 The results of the second test: (a) DG1 output currents; (b) DG1 fundamental positive sequence currents; (c) DG2 output currents; (d) DG2 fundamental positive sequence currents
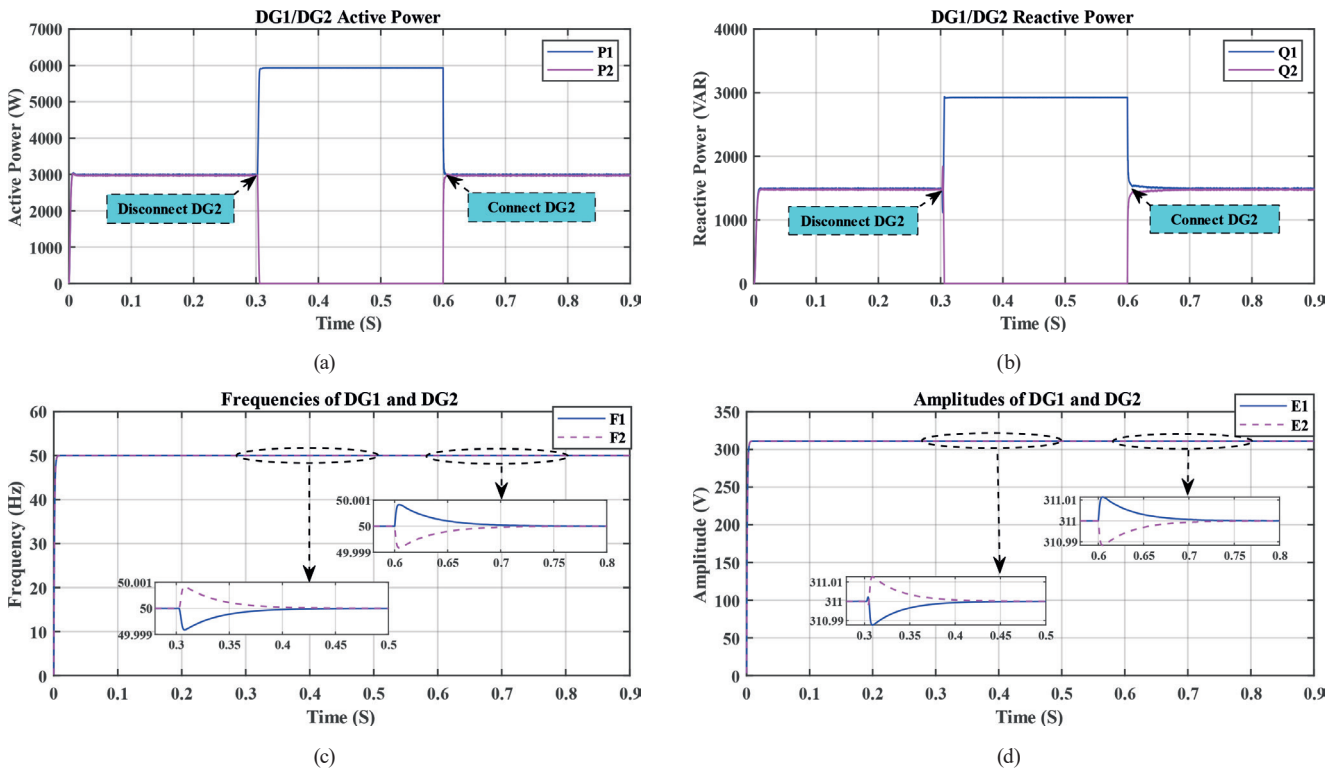

Fig. 14 The results of the third test: (a) DG1/DG2 active power; (b) DG1/DG2 reactive power; (c) Frequencies of DG1 and DG2; (d) Amplitudes of DG1 and DG2

an increase in reactive power corresponds to a decrease in amplitude voltage, and vice versa.

5 Conclusion

This paper introduces an innovative droop control technique aimed at regulating power delivery from parallel DG inverters and achieving stable voltage at the connected common-coupled AC bus. The main goal of this method is to address frequency and amplitude deviations in the output voltage caused by changes in load power, effectively tackling these issues compared to conventional droop control. Moreover, the current extraction technique is leveraged to introduce selective virtual impedance at fundamental positive, fundamental negative, and harmonic frequencies in the microgrid. This approach effectively tackles line impedance mismatch, enhances load sharing among DG sources, and improves the performance of droop controllers. By implementing positive-sequence virtual impedance, the microgrid ensures balanced load sharing, while negative-sequence virtual impedance works to minimize negative-sequence circulating currents and compensate for voltage distortion. Furthermore, the virtual variable harmonic impedance loop facilitates the sharing of harmonic power, leading to an overall improvement in power quality within the microgrid.

References

[1] Ellabban, O., Abu-Rub, H., Blaabjerg, F. "Renewable energy resources: Current status, future prospects and their enabling technology", Renewable and Sustainable Energy Reviews, 39, pp. 748–764, 2014.
https://doi.org/10.1016/j.rser.2014.07.113

[2] Satish, B., Bhuvaneswari, S. "Control of microgrid: a review", In: 2014 International Conference on Advances in Green Energy (ICAGE), Thiruvananthapuram, India, 2014, pp. 18–25. ISBN 9781479980505
https://doi.org/10.1109/ICAGE.2014.7050138

[3] Villeneuve, P. L. "Concerns generated by islanding", IEEE Power and Energy Magazine, 2(3), pp. 49–53, 2004.
https://doi.org/10.1109/mpae.2004.1293600

[4] Chen, J. F., Chu, C.-L. "Combination voltage-controlled and current-controlled PWM inverters for UPS parallel operation", IEEE Transactions on Power Electronics, 10(5), pp. 547–558, 1995.
https://doi.org/10.1109/63.406842

[5] Lee, C. S., Kim, S., Kim, C. B., Hong, S. C., Yoo, J. S., Kim, S. W., Kim, C. H., Woo, S. H., Sun, S. Y. "Parallel U.P.S. with a instantaneous current sharing control", In: 1998 Proceedings of the 24th Annual Conference of the IEEE Industrial Electronics Society (Cat. No. 98CH36200), Aachen, Germany, 1998, pp. 568–573. ISBN 0-7803-4503-7
https://doi.org/10.1109/iecon.1998.724306

[6] Van Der Broeck, H., Boeke, U. "A simple method for parallel operation of inverters", In: INTELEC-Twentieth International Telecommunications Energy Conference (Cat. No.98CH36263), San Francisco, CA, USA, 1998, pp. 143–150. ISBN 0-7803-5069-3
https://doi.org/10.1109/intlec.1998.793490

[7] Pei, Y., Jiang, G., Yang, X., Wang, Z. "Auto-master-slave control technique of parallel inverters in distributed AC power systems and UPS", In: 2004 IEEE 35th Annual Power Electronics Specialists Conference, Aachen, Germany, 2004, pp. 2050–2053. ISBN 0-7803-8399-0
https://doi.org/10.1109/pesc.2004.1355433

[8] Chen, Y.-K., Wu, T.-F., Wu, Y.-E., Ku, C.-P. "A current-sharing control strategy for paralleled multi-inverter systems using microprocessor-based robust control", In: 2001 Proceedings of IEEE Region 10 International Conference on Electrical and Electronic Technology (TENCON), Singapore, 2001, pp. 647–653. ISBN 0-7803-7101-1
https://doi.org/10.1109/tencon.2001.949673

[9] Xing, Y., Huang, L., Sun, S., Yan, Y. "Novel control for redundant parallel UPSs with instantaneous current sharing", In: 2002 Proceedings of the Power Conversion Conference, Osaka, Japan, 2002, pp. 959–963. ISBN 0-7803-7156-9
https://doi.org/10.1109/pcc.2002.998098

[10] Sun, X., Lee, Y.-S., Xu, D. "Modeling, analysis, and implementation of parallel multi-inverter systems with instantaneous average-current-sharing scheme", IEEE Transactions on Power Electronics, 18(3), pp. 844–856, 2003.
https://doi.org/10.1109/tpel.2003.810867

[11] Wu, T.-F., Chen, Y.-K., Huang, Y.-H. "3C strategy for inverters in parallel operation achieving an equal current distribution", IEEE Transactions on Industrial Electronics, 47(2), pp. 273–281, 2000.
https://doi.org/10.1109/41.836342

[12] Yao, W., Chen, M., Chen, J., Qian, Z. "An improved multiple-loop controller for parallel operation of single-phase inverters with no control interconnections", In: 2007 IEEE Power Electronics Specialists Conference, Orlando, FL, USA, 2007, pp. 448–452. ISBN 978-1-4244-0654-8
https://doi.org/10.1109/pesc.2007.4342029

[13] Guerrero, J. M., Vicuna, L. G. D., Matas, J., Castilla, M., Miret, J. "Output impedance design of parallel-connected UPS inverters with wireless load-sharing control", IEEE Transactions on Industrial Electronics, 52(4), pp. 1126–1135, 2005.
https://doi.org/10.1109/tie.2005.851634

[14] Feddaoui, O., Toufouti, R., Djamel, L. "Active and reactive power sharing in micro grid using droop control", International Journal of Electrical and Computer Engineering (IJECE), 10(3), pp. 2235–2244, 2020.
https://doi.org/10.11591/ijece.v10i3.pp2235-2244

[15] Guerrero, J. M., Matas, J., Vicuna, L. G. D., Castilla, M., Miret, J. "Wireless-Control Strategy for Parallel Operation of Distributed-Generation Inverters", IEEE Transactions on Industrial Electronics, 53(5), pp. 1461–1470, 2006.
https://doi.org/10.1109/tie.2006.882015

[16] Li, Y. W., and Kao, C.-N. "An accurate power control strategy for power-electronics-interfaced distributed generation units operating in a low-voltage multibus microgrid", IEEE Transactions on Power Electronics, 24(12), pp. 2977–2988, 2009.
https://doi.org/10.1109/tpel.2009.2022828

[17] Pompodakis, E. E., Tinajero, G. D. A., Karapidakis, E. S. "Modelling the steady-state of secondary control in islanded AC microgrids", International Journal of Electrical Power and Energy Systems, 153, 109295, 2023.
https://doi.org/10.1016/j.ijepes.2023.109295

[18] Yao, W., Chen, M., Matas, J., Guerrero, J. M., Qian, Z.-M. "Design and Analysis of the Droop Control Method for Parallel Inverters Considering the Impact of the Complex Impedance on the Power Sharing", IEEE Transactions on Industrial Electronics, 58(2), pp. 576–588, 2011.
https://doi.org/10.1109/tie.2010.2046001

[19] Rodriguez, P., Luna, A., Candela, I., Mujal, R., Teodorescu, R., Blaabjerg, F. "Multiresonant Frequency-Locked Loop for Grid Synchronization of Power Converters Under Distorted Grid Conditions", IEEE Transactions on Industrial Electronics, 58(1), pp. 127–138, 2011.
https://doi.org/10.1109/tie.2010.2042420

[20] Ren, X., Lyu, Z., Li, D., Zhang, Z., Zhang, S. "Synchronization signal extraction method based on enhanced DSSOGI-FLL in power grid distortion", Systems Science & Control Engineering, 6(3), pp. 305–313, 2018.
https://doi.org/10.1080/21642583.2018.1554843

[21] Han, Y., Shen, P., Zhao, X., Guerrero, J. M. "An Enhanced Power Sharing Scheme for Voltage Unbalance and Harmonics Compensation in an Islanded AC Microgrid", IEEE Transactions on Energy Conversion, 31(3), pp. 1037–1050, 2016.
https://doi.org/10.1109/tec.2016.2552497

[22] Abusara, M. A., Sharkh, S. M., Guerrero, J. M. "Improved droop control strategy for grid-connected inverters", Sustainable Energy, Grids and Networks, 1, pp. 10–19, 2015.
https://doi.org/10.1016/j.segan.2014.10.002

[23] Ranjbaran, A., Ebadian, M. "A power sharing scheme for voltage unbalance and harmonics compensation in an islanded microgrid", Electric Power Systems Research, 155, pp. 153–163, 2018.
https://doi.org/10.1016/j.epsr.2017.09.026

[24] Mohammed, N., Ali, M., Ciobotaru, M., Fletcher, J. "Accurate control of virtual oscillator-controlled islanded AC microgrids", Electric Power Systems Research, 214, 108791, 2023.
https://doi.org/10.1016/j.epsr.2022.108791

[25] Tayab, U. B., Roslan, M. A. B., Hwai, L. J., Kashif, M. "A review of droop control techniques for microgrid", Renewable and Sustainable Energy Reviews, 76, pp. 717–727, 2017.
https://doi.org/10.1016/j.rser.2017.03.028

[26] Grairia, M. I., Toufouti, R. "Finite Control Set MPC for Voltage and Frequency Stabilization in Islanded AC Microgrids with Line Impedance Consideration and Enhanced Power Sharing Control", Journal Européen des Systèmes Automatisés, 56(2), pp. 291–300, 2023.
https://doi.org/10.18280/jesa.560214

Appendix

Table A1 Microgrid parameter values

System parameter	Value
DC link voltage	650 V
LCr-filter	$L = 3$ mH, $C = 50$ µF, $r = 1$ mΩ
Amplitude (phase to ground)	$E = 311$ V
Frequency	$F = 50$ Hz
DG feeder	DG1: $R_{f1} = 0.4$ Ω, $L_{f1} = 2$ mH DG2: $R_{f2} = 0.2$ Ω, $L_{f2} = 1$ mH
Proposed droop control	**Value**
Frequency droop coefficient	$k_f = 1 \times 10^{-4}$
Amplitude droop coefficient	$k_v = 3 \times 10^{-4}$
Integral frequency coefficient	$k_m = 1000$
Integral amplitude coefficient	$k_n = 1000$
Voltage and current control	**Value**
Proportional voltage gain	$k_{vp} = 150$
Integral voltage gain	$k_{vi} = 50$
Proportional current gain	$k_{ip} = 60$
Switching frequency	$F_{sw} = 10$ kHz
Selective virtual impedance	**Value**
Virtual inductance	DG1: $L_{v1} = 0$ mH DG2: $L_{v2} = 1$ mH
Positive virtual resistance	DG1: $R_{vf1}^{+} = 0$ Ω DG2: $R_{vf2}^{+} = 0.2$ Ω